The Astrophysical Journal, 631:976–987, 2005 October 1

PRESOLAR GRAPHITE FROM AGB STARS: MICROSTRUCTURE AND *s*-PROCESS ENRICHMENT

Thomas K. Croat, Frank J. Stadermann, and Thomas J. Bernatowicz
Department of Physics and Laboratory for Space Sciences, Washington University,
Campus Box 1105, One Brookings Drive, St. Louis, MO 63130-4899
Received 2005 March 8; accepted 2005 April 12

ABSTRACT

Correlated transmission electron microscopy and secondary ion mass spectrometry with submicron spatial resolution (NanoSIMS) investigations of the same presolar graphites spherules from the Murchison meteorite were conducted, to link the isotopic anomalies with the mineralogy and chemical composition of the graphite and its internal grains. Refractory carbide grains (especially titanium carbide) are commonly found within the graphite spherules, and most have significant concentrations of Zr, Mo, and Ru in solid solution, elements primarily produced by *s*-process nucleosynthesis. The effect of chemical fractionation on the Mo/Ti ratio in these carbides is limited, and therefore from this ratio one can infer the degree of *s*-process enrichment in the gas from which the graphite condensed. The resulting *s*-process enrichments within carbides are large (~200 times solar on average), showing that most of the carbide-containing graphites formed in the mass outflows of asymptotic giant branch (AGB) stars. NanoSIMS measurements of these graphites also show isotopically light carbon (mostly in the $100 < {}^{12}C/{}^{13}C < 400$ range). The enrichment of these presolar graphites in both *s*-process elements and ^{12}C considerably exceeds that astronomically observed around carbon stars. However, a natural correlation exists between ^{12}C and *s*-process elements, as both form in the He intershell region of thermally pulsing AGB stars and are dredged up together to the surface. Their observation together suggests that these graphites may have formed in chemically and isotopically inhomogeneous regions around AGB stars, such as high-density knots or jets. As shown in the companion paper, a gas density exceeding that expected for smooth mass outflows is required for graphite of the observed size to condense at all in circumstellar environments, and the spatially inhomogeneous, high-density regions from which they condense may also be incompletely mixed with the surrounding gas. We have greatly expanded the available data set of presolar graphites ($N = 847$) and characterized them by their morphology (onion type and cauliflower type). This effort has also revealed two new, rare presolar phases (iron carbide and metallic osmium). Due to the peculiar gas composition needed to form these rare presolar grain types, the graphites containing them are more likely to originate in supernova outflows.

Subject headings: dust, extinction — nuclear reactions, nucleosynthesis, abundances — stars: AGB and post-AGB

Online material: color figures

1. INTRODUCTION

Recent improvements in microanalytical techniques, mainly in the coordinated use of transmission electron microscopy (TEM) and new secondary ion mass spectrometry with nanometer-scale spatial resolution (NanoSIMS), have made possible detailed investigations of micron-sized presolar grains, which are condensates formed in the mass outflows from stars predating the solar system and that are found in primitive meteorites and interplanetary dust particles. The chemical, isotopic, and microstructural information preserved in these grains can be extracted with TEM and NanoSIMS analyses and used to form a more detailed and accurate picture of grain condensation in stellar outflows. The isotopic compositions of individual presolar grains often permit inferences as to the types of stellar sources that produced them, such as asymptotic giant branch (AGB) stars and supernovae. The microstructure and chemical composition of presolar grains, and of subgrains of other phases commonly found within them, add further detail to the condensation process. The sequence of phase condensation, as inferred from the observed microstructure, can be used to guide modeling efforts that place constraints on the pressure and composition of the gaseous outflows from which the grains condensed. The study of presolar grains has advanced from the initial discovery of these isotopic curiosities to its current state in which detailed histories of the formation of individual grains can be constructed, often giving insight into astrophysical processes that are unavailable through astronomical observation alone (Clayton & Nittler 2004; Zinner 1998).

Laboratory microanalysis can result in new, direct information on the types of presolar grains that form (and their size and microstructure), giving new insights into grain condensation around stars. For example, the discovery of titanium carbides (TiCs) with attached metallic iron subgrains encapsulated within graphites of supernova (SN) origin allows the sequence of phase condensation in the SN ejecta to be inferred (Croat et al. 2003). Interpreted by thermochemical models, the condensation sequence (TiC → metallic iron → graphite) implies relatively high iron abundance in the part of the SN outflow where the grain condensed. Extensive studies of single presolar SN graphites, some of which contain hundreds of internal carbides entrained during their growth, reveal specific details about their condensation history. Trends in the size and chemical composition of internal carbides versus radial distance (an indication of the time of condensation) show progressive equilibration with the surrounding gas and indicate that carbides cease growing when encapsulated by graphite.

Bernatowicz et al. (1996) conducted an isotopic and microstructural study of presolar graphite spherules from the KFC1 density separate (2.15–2.20 g cm^{-3}, >1 μm diameter) from the

Murchison meteorite. Secondary ion mass spectrometry (SIMS) of the graphites showed a wide range of carbon isotopic ratios, ranging over 3 orders of magnitude from 0.02 to 80 times the solar value of 89. Two different spherule types were investigated, designated "onion" and "cauliflower" based on external morphology in scanning electron microscope (SEM) images. TEM images of ultramicrotomed slices of the graphite spherules showed that structural differences, in the regularity and long-range continuity of the stacking of graphene sheets, led to distinct external morphologies for the onion and cauliflower types. In addition, the cores of most onion graphites were found to be nanocrystalline, consisting of small randomly oriented domains of carbon in graphene sheets. The exteriors of these onion graphites were well-crystallized graphitic layers, which formed concentric shells around the nanocrystalline cores. Internal grains, mostly refractory titanium carbides, were also found inside some sliced graphites. Many of these carbides showed large enrichments above the solar ratios in Zr, Mo, and Ru, elements predominantly produced by the *s*-process nucleosynthesis. Due to instrumental limitations in the Bernatowicz et al. (1996) study, both isotopic and TEM results could not be obtained from the same individual graphite spherules, only from different graphites from the same population.

In this study, combined isotopic and TEM investigations have been made on the *same* individual micron-sized graphites from KFC1, using the improved sensitivity and spatial resolution of the NanoSIMS, which makes high spatial resolution isotopic measurements of ultramicrotomed graphite slices ($\sim$70 nm thick) possible. We have completed TEM analysis of many KFC1 graphites ($N = 847$) and performed subsequent NanoSIMS isotopic analysis on a subset of these ($N = 133$), greatly expanding the data set on KFC1 presolar graphites and permitting a coordinated isotopic and microstructural study of individual grains. The types of presolar graphites found within Murchison meteorite KFC1 residue are classified by their morphology and microtexture. The size distributions and relative abundance of various graphite types are also presented. This paper focuses on the onion-type graphites, both on their internal structure and on internal high-temperature condensate grains that were captured by the graphites during their growth. Careful attention is paid to the chemical composition of refractory carbides, especially to the *s*-process elements Zr, Mo, and Ru. The influence of chemical fractionation on the carbide composition is investigated in order to deconvolve its effect from the overall *s*-process enrichment in the gas from which the grain condensed. As discussed below and in the companion paper (Bernatowicz et al. 2005, hereafter Paper II), the stellar sources of most KFC1 graphites appear to be AGB carbon stars. Carbon and oxygen isotopic ratios are presented for individual carbide-containing graphites. The examination of larger numbers of presolar grains in this study has also led to the discovery of rare and new presolar grain types, such as the kamacite, iron carbide, and metallic osmium phases reported here.

2. SAMPLES AND EXPERIMENTAL METHODS

Graphites from the KFC1 density and size separate (2.15–2.20 g cm^{-3}, >1 μm) of the Murchison meteorite were embedded in resin and sliced into <100 nm thick sections (details in Amari et al. 1994 and Bernatowicz et al. 1996). Sliced graphites were examined in a JEOL-2000FX TEM equipped with a NORAN energy dispersive X-ray spectrometer (EDXS). Selected-area diffraction (SAD) patterns and bright- and dark-field images were used to better characterize the structural differences between the graphite types. Dark-field {002} images (created from the electrons diffracted by the {002} crystal planes rather than the direct electron beam) were used to determine the size of ordered structural domains, which was central in graphite classification. Both onion-type and cauliflower-type KFC1 graphites often captured and preserved other higher temperature stellar condensates during their growth, and these internal grains give further important clues about grain condensation in stellar outflows. Therefore, graphites were searched for internal grains by observation at high magnifications ($\sim 10^5$) during tilting of the specimen stage, and grains as small as 5 nm became clearly visible when in an orientation satisfying the Bragg diffraction condition (for further details, see Croat et al. 2003). A small subset of graphites ($N = 31$) from the earlier TEM study (Bernatowicz et al. 1996) was reexamined to ensure consistency of experimental methods.

EDXS spectra allowed identification of elemental peaks (with $Z \geq 5$), although attention to possible overlapping peaks or artifacts was essential. Fits of the EDXS background over peak regions of interest were done with polynomial functions. For single peaks with no overlap, the peak counts remaining after background subtraction were directly integrated. In cases of overlap, peaks were first fit with multiple Gaussians with the peak energies and relative magnitudes constrained by those seen in pure standards. Fitting results were also checked with another EDXS software package (NORAN Vantage). Quantitative analysis was then done using *k*-factors derived from geological standards (chromite USNM 117075, ilmenite USNM 96189, basaltic glass USNM 113498) and numerous stoichiometric oxides (lead titanate, lead zirconate, lead molybdate, calcium vanadate, calcium titanate, calcium phosphate, etc.). Standards for all elements (except Os and Ru) fixed elemental ratios to Ti (the dominant element in most internal grains), typically with a 3%–6% variation in the derived *k*-factor. The overall error (from both the *k*-factor error and from 2 σ counting statistical errors) varied among the grains, depending mostly on the grain size, which determines the attainable EDXS count rate. In some cases, only upper limits were determined for elements that were not detected. A value of 2 σ of the background counts near the energy of each elemental line was used as the upper limit for counts, because concentrations above this limit would be clearly visible. The longer EDXS count times and quantitative analysis with standards employed in this study allowed more accurate determinations of chemical composition.

The crystal structures of internal grains were determined from multiple SAD and/or microdiffraction patterns, typically using 3–4 major zone axis patterns for unknown phases. The diffraction rings from {100} and {110} graphite served as an internal calibration for *d*-spacings ($\sim$1% accuracy), as well as for astigmatism correction. Angles between zone axis patterns were checked for consistency with known crystal structures. For common phases (e.g., TiC), often a single cubic diffraction pattern from a low-index zone combined with the EDXS composition were sufficient for identification. In cases of internal grains with attached subgrains, an orientation relationship was sought, e.g., an alignment between low-index crystallographic zones that is commonly seen in cases of epitaxial growth.

After TEM microstructural analysis, a TEM grid containing hundreds of sliced graphites was mounted on a conducting substrate and analyzed in the NanoSIMS. A Cs^+ primary beam of $\sim$100 nm diameter was rastered over the samples while secondary electrons and negative secondary ions ($^{12}C^-$, $^{13}C^-$, $^{16}O^-$, $^{18}O^-$, and $^{28}Si^-$) were collected simultaneously. Isotopic ratios for carbon and oxygen determined in many graphites were found to be consistent with earlier SIMS measurements on graphites from the same KFC1 fraction of Murchison; the carbon isotopic ratios are reproduced in Figure 1 from Amari et al. (1993) and Hoppe et al. (1995) for the benefit of the reader. The nearby carbon film on the TEM grid provided a standard with which to

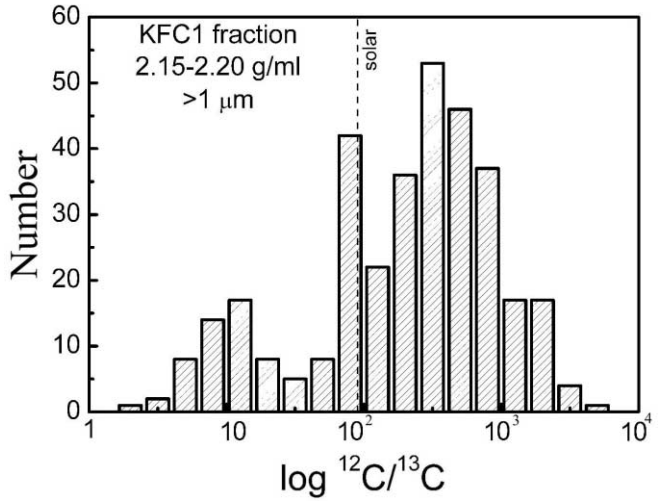

FIG. 1.—Histogram of $^{12}C/^{13}C$ isotopic ratios from all KFC1 graphites measured with the Cameca IMS3f ion microprobe, showing a roughly bimodal distribution and a dearth of grains in the $^{12}C/^{13}C = 30-70$ range. Data are reproduced from Amari et al. (1993) and Hoppe et al. (1995).

calibrate C and O ratios. Further experimental details are found in Stadermann et al. (2005).

3. RESULTS

3.1. *Morphology and Microtexture of Graphite Spherules*

Imaging and diffraction in the TEM provide morphological, structural, and microtextural information on graphite spherules, and thus a brief explanation of the graphite structure is required to move beyond characterization of onion and cauliflower graphites based on surface morphology alone. Graphite is composed of carbon bonded in a hexagonal network, forming two-dimensional graphene sheets. These sheets are then stacked to form the basic structural unit (BSU) of graphite, which can be characterized by the overall height of the stacked sheets along the *c*-axis (L_c) and also the lateral extent of the sheets in the basal plane (L_a). Variations in the interplanar spacing as well as curvature and crumpling of the sheets are also possible. The commonly known crystal structure of graphite consists of graphene sheets stacked in a layered ABABAB... sequence along the *c*-axis in the ideal hexagonal structure ($a = 2.46$ Å, $c = 6.7$ Å), which is essentially a graphite composed of a single BSU. However, the term "graphite" is used more loosely for any carbon structure built up from smaller BSUs. The relatively weak bonding between the graphene sheets and the insertion of pentagons in the basal plane hexagonal structure allows for many observed graphite morphologies (e.g., graphite spherules, platelike graphite in metamorphic rocks, filamentous graphites such as carbon nanotubes and graphite whiskers, and C_{60} and other fullerenes; Jaszczak 1995). These structures are differentiated based on both external morphology and on microtexture, which describes the local ordering of adjacent BSUs.

Many graphites ($N = 847$) from the KFC1 residue were examined, most of which were spherule cross sections. The spherules were identified as graphite from the {100} and {110} diffraction rings characteristic of graphene sheets. Further distinctions among graphite subtypes were made using bright-field and dark-field imaging, especially {002} dark-field images, which can reveal the microtexture. Along with onion and cauliflower graphites, other graphite morphologies are also present in the residue, including crystalline graphites with discrete diffraction spots instead of rings, aggregates of multiple spherules (e.g., multiple onion graphites aggregated into a larger composite graphite), fragments of larger graphites too incomplete to classify, and other graphites often intermediate in apparent density or lacking a clear concentric structure. Preliminary isotopic analyses of graphites from each type with the NanoSIMS suggest that all are presolar except for the crystalline ones. Figure 2 shows bright-field images from

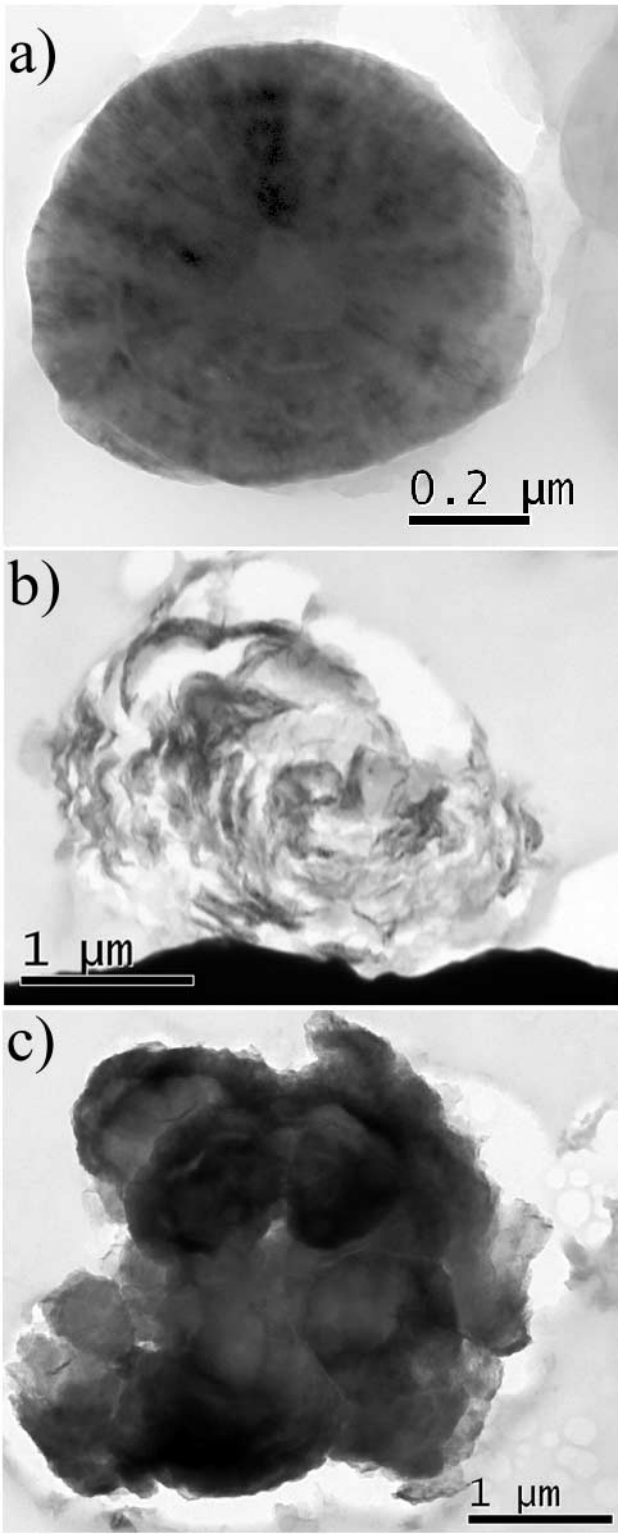

FIG. 2.—Bright-field TEM images of typical examples of (*a*) onion, (*b*) cauliflower, and (*c*) aggregate graphites. The aggregate graphite appears to be composed of four or more separate onion-like graphites.

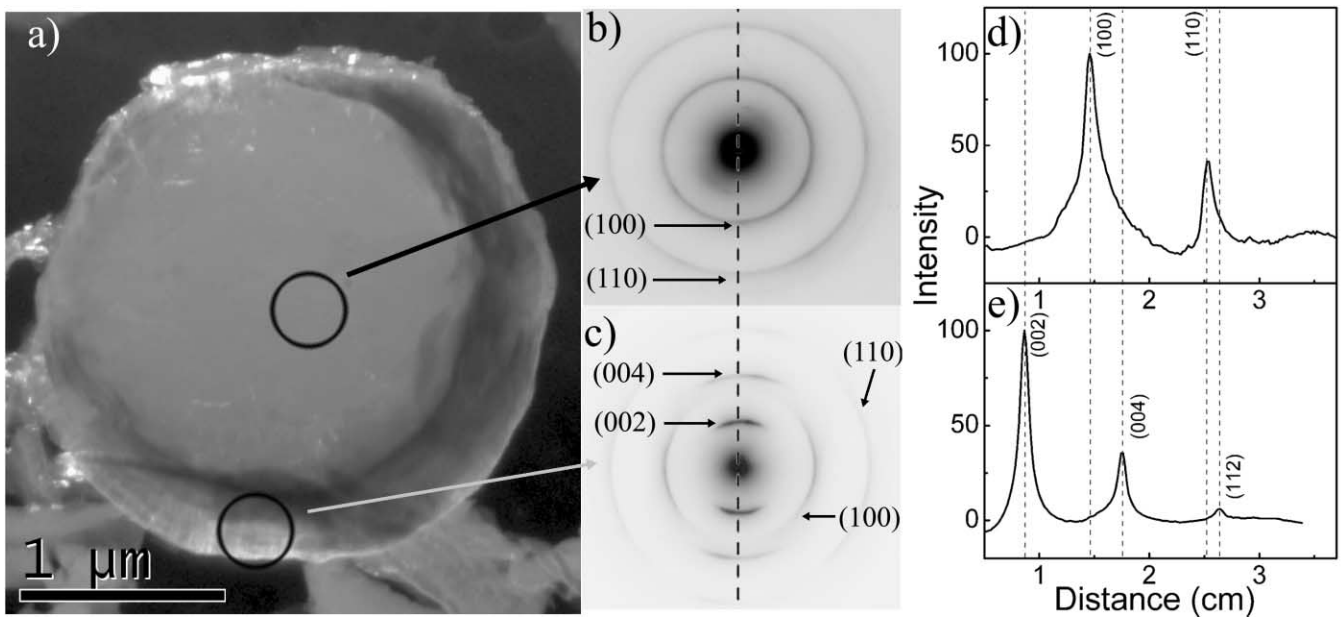

FIG. 3.—(*a*) Dark-field {002} image of a rim-core onion graphite, along with (*b*, *c*) SAD patterns taken from separate ≈300 nm regions (circled in image). (*d*, *e*) Line profiles of the diffracted intensity were taken from the digitized SAD patterns (along the dotted vertical lines), and major diffraction peaks are indexed with the family of planes (*hkl*) from the known graphite structure.

typical examples of onion, cauliflower, and aggregate graphites. Despite similar thickness, the onion graphites (Fig. 2*a*) are considerably darker than cauliflowers in bright-field images due to strong electron scattering from the well-crystallized layers. SAD patterns from onion layers (as in Fig. 3*c*) show strong {002} rings formed from planes of atoms in BSUs all viewed edge-on (with their *c*-axis perpendicular to the electron beam). The {002} diffracted intensity is strongly peaked in a direction perpendicular to the layers in the image, showing strong texturing of BSUs within the onion layers with most of the BSUs lying flat on the spherule surface. Lower magnification dark-field images show that the layers are coarsely aligned over hundreds of nanometers, gradually curving to form the concentric layers of the onion. Most of the onion graphites have nanocrystalline cores, which will be discussed in more detail in § 3.3. Cauliflower graphites (Fig. 2*b*) have turbostratic layering, which consists of graphene sheets that are wavy and contorted. Some do show a roughly concentric structure with layers that diffract coherently over several hundred nanometers in the L_a direction. Unlike onions though, these coherently scattering domains are of limited thickness ($L_c < 50$ nm). The lack of orderly stacking in the *c*-axis direction leads to looser packed structures, with gaps visible (10%–15% missing) in the cross sections and apparently lower density than onion-type graphites. Other cauliflowers are even less textured, being devoid of concentric layers and consisting of coherent-scattering domains with a maximum diameter of 20–30 nm. The {002} diffraction rings in SAD patterns of cauliflowers appear to be more isotropic, due to the weaker texturing of the BSUs within the ~300 nm selected area. The *c*-direction spacing as measured from the {002} diffraction ring (with {100} used as an internal calibration) is 3.54 ± 0.06 Å and appears similar in onions and cauliflowers. Aggregate graphites (Fig. 2*c*) are composite objects formed when multiple graphites that apparently originally nucleated and grew separately became attached and were cemented together by further graphite growth.

3.2. *Relative Abundance and Size*

Table 1 summarizes the number of graphite spherules of each type studied in the TEM, and these roughly reflect the abundance of each type in the KFC1 residue. Data for the onions are also split into two subgroups, depending on the presence or absence of a nanocrystalline core at the spherule center. The relative abundance of onions in the KFC1 residue as defined here is lower than in earlier SEM- based classifications (Hoppe et al. 1995). Since the degree of texturing varies somewhat continuously between onions and cauliflowers, the division between the groups is

TABLE 1
ABUNDANCE AND SIZE OF KFC1 GRAPHITES BY TYPE

GRAPHITE TYPE	NUMBER	PERCENT OF OVERALL POPULATION	GEOMETRICAL MEAN DIAMETER (μm)		
			Average	Standard Deviation	Range (Minimum–Maximum)
Onion	340	40	1.18	0.64	0.23–4.20
Onion with nanocrystal core	228	27	1.35	0.65	0.43–4.20
Onion without core	109	13	0.95	0.54	0.23–2.80
Cauliflower	241	29	2.40	0.96	0.88–4.68
All other types	266	31	1.60	0.82	0.34–4.61

NOTES.—Shown are the number, abundance, and size of the various graphite types found in the Murchison KFC1 residue. Onion graphites are split into subgroups depending on the presence or absence of a nanocrystalline core at their center.

somewhat subjective. We feel that characterization based on the morphology and microtexture of cross sections with TEM (as described in the previous section) is more reliable than that based on surface morphology alone. The presence of cauliflowers with apparent lower density (gaps within the internal structure) is somewhat unexpected in the dense KFC1 fraction (2.15–2.20 g cm^{-3}). However, larger, less dense grains, such as the 2.2 μm median diameter cauliflowers, diffuse more slowly ($D \propto 1/R$, as described by Stokes-Einstein relation), making them more difficult to separate during centrifugation. The turbostratic layering, microtexture in dark-field imaging, and apparent lower density of cauliflowers make them morphologically similar to the supernova graphites from the Murchison KE3 graphite separate (Amari et al. 1994) previously investigated by Croat et al. (2003). However the KFC1 cauliflowers lack the oxygen isotopic anomalies commonly seen in the KE3 SN graphites, suggesting a fundamental difference in the stellar sources of these morphologically similar graphites. This difference is still being investigated as the subject of further isotopic studies, and in the remainder of this paper we concentrate on the onion graphites.

In Table 1 the original graphite diameter was inferred from the diameter of a single slice assuming that it came from near the center. Such an assumption will often underestimate the true diameter, as slices were effectively taken through collections of graphite grains and thus at a random height for any individual grain that will seldom intercept the maximum dimension. The average apparent onion graphite diameter of $\sim$1.2 μm (from Table 1) is thus less than the average graphite diameter before slicing. The mean diameter of the original distribution is not available from SEM images, as the classification of onions from surface morphology is unclear. If we assume a lognormal grain size distribution (commonly used for grains condensed from a gas) and that slices are made at a random distance from the graphite center, we can infer the original onion size distribution. A lognormal distribution with a mean size of 2 μm and $\sigma = 2.8$ matches the observed onion size distribution well if sliced at random heights, so it is likely that the original size distribution was similar. It was also determined that the observed distribution cannot be reproduced by slicing of a monodispersed population or other populations that are not as sharply peaked as the lognormal distribution. The significant observed fraction of submicron-sized onions (47% of the sliced population) does not indicate that the intended >1 μm size separation failed, but rather that many apparently smaller diameter onions are a result of slicing. The cauliflower and the aggregate graphites are clearly larger than the onions. Using a similar analysis as above, a lognormal distribution with a 6 μm mean size ($\sigma = 2.7$) matches the observed distribution of cauliflower diameters. The size of aggregate graphites is quite similar to the cauliflowers, although the uncertainty is greater due to fewer available grains.

3.3. *Structure of Rim-Core Onions*

As mentioned previously, roughly two-thirds of the onion graphites have nanocrystalline cores at their centers. Figure 3 shows a dark-field {002} image of a typical rim-core graphite along with separate SAD patterns taken from the core region (Fig. 3*b*) and from the graphitic rim (Fig. 3*c*). Line profiles of the SAD intensity (Figs. 3*d* and 3*e*) are also shown (taken along the dashed vertical lines in Figs. 3*b* and 3*c*), and the major peaks are indexed with the crystal planes that produced them. The nanocrystalline core (Figs. 3*b* and 3*d*) does not show {002} or other higher order reflections from stacking of layers along the *c*-axis, instead showing only {100}, {110}, and other {*hk*0} peaks. This clearly demonstrates a lack of ordered stacking (even on the local level). Extensive analysis and simulation of diffraction data suggest that the cores consist of randomly oriented $\leq$4 nm curved and convoluted graphene sheets with no regular *c*-axis stacking, which thus are nanocrystalline (Bernatowicz et al. 1996; Fraundorf & Wackenhut 2002). There also are present much smaller ($\sim$1 nm) PAH-like units that broaden the base of the diffraction peaks. In contrast, the graphitic spherule rims (Figs. 3*c* and 3*e*) produce strong {002} and {004} peaks in a direction perpendicular to the graphitic layers in the image.

The graphite rims could conceivably result from a later transformation of the core material (through thermal annealing or irradiation). However, as discussed in Bernatowicz et al. (1996), it is unlikely that any thermal annealing would be able to graphitize only part of the core into a rim (as is observed) and leave a sharp transition between the two regions. Particle irradiation can also graphitize amorphous carbon given sufficient flux, but again would likely result in sufficient local heating to transform the entire graphite. The remaining, and more likely, possibility is that the graphitic rims were vapor deposited onto the nanocrystalline cores and progressive changes in the gas altered the degree of crystallinity of the deposited carbon. As noted in Bernatowicz et al. (1996), the nanocrystalline cores have the characteristics of material condensed from a supersaturated state. They speculated that the nanocrystals may have physically accreted after rapid nucleation to form cores that were subsequently overgrown by more slowly deposited graphite as the pressure dropped in the grain formation region.

3.4. *Internal Grains within Onion Graphites*

Refractory carbides were commonly found within onion graphites, a total of 111 carbides within 47 different onions. Figure 4 shows examples of carbide-containing graphites (one with a central crystal and another with multiple noncentral crystals) as well as another graphite with an internal grain of a different phase (metallic osmium, as discussed later). The carbides were found within 16% of onion graphites, and they were twice as likely to be found in highly graphitic onions as in onions with nanocrystalline cores. The true fraction of graphites containing carbides is clearly higher, because only a single slice from each spherule was examined (comprising $\sim$5%–10% of its entire volume). The measured carbide abundance relative to graphite (derived from an areal fraction in cross sections) is quite variable, ranging from 100 to 47,000 ppm (parts per million), with a global average of $\sim$1300 ppm in carbide-containing onions. Given this average abundance, the majority of graphites probably contain carbides, but this fraction cannot be accurately determined after slicing. Textural evidence as well as compositional variation among carbides within a single graphite indicate that carbides formed first and were then incorporated into the graphite, rather than forming later by exsolution (Bernatowicz et al. 1996; Croat et al. 2003). These high-temperature condensates were ubiquitous in the gas at the time that graphites began to form. About 40% of the carbide-containing graphites had an internal grain located at the spherule center (as in Fig. 4*a*). This is taken as an indication of heterogeneous nucleation of graphite on the carbide. With our current method, we cannot exactly determine how common this is, or whether some graphites nucleated homogeneously directly from the gas. The presence of such heterogeneous nucleation centers would affect the degree of supersaturation prior to graphite formation, which could affect the graphite morphology.

The size of the internal carbides has important implications for the number density of various species in the gas from which they

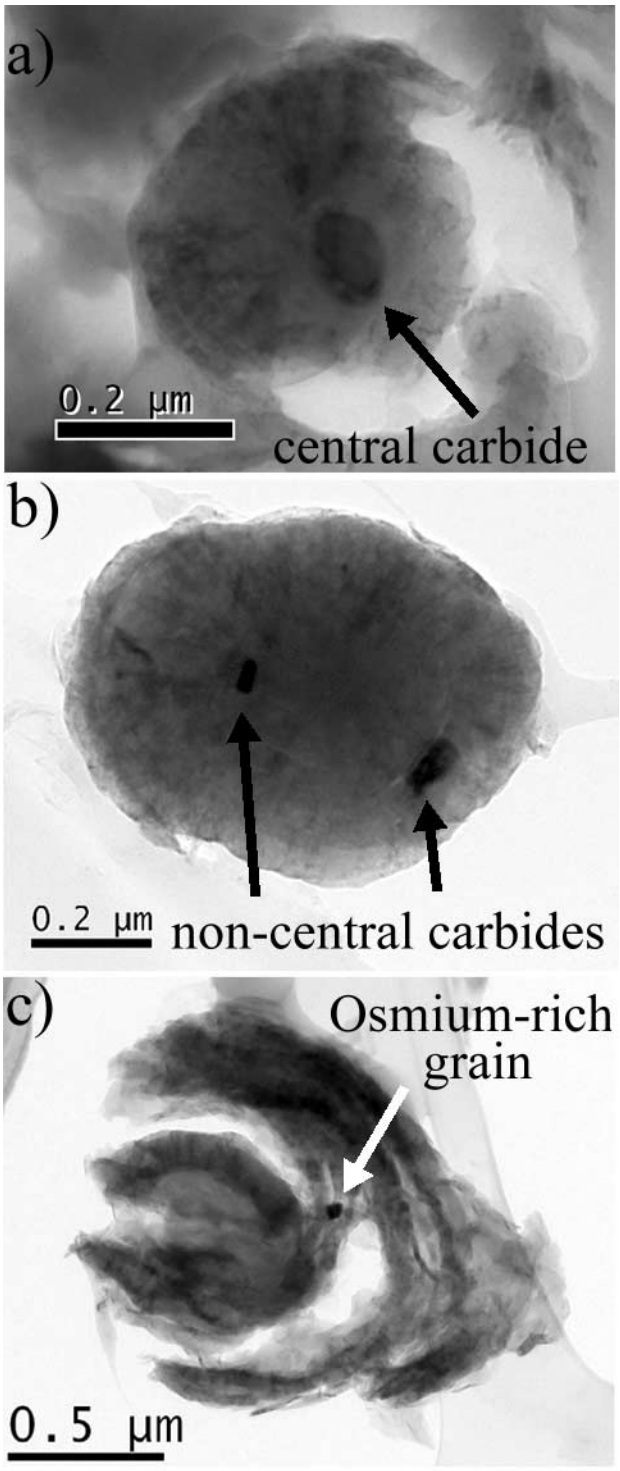

FIG. 4.—Bright-field TEM images of onion-type graphites containing internal grains: (*a*) central TiC that likely served as a nucleation center for graphite, (*b*) multiple Zr-rich noncentral carbides, and (*c*) ~50 nm metallic osmium grain.

condensed. Figure 5 shows the size distribution of carbides from onion-type graphites, with an average geometrical mean size of 24 nm and a range of 7–90 nm. Since the carbides are generally smaller than a typical slice thickness (~75 nm), the size distributions are basically unmodified by slicing. The carbides within KFC1 onion-type graphites are about ~5 times smaller than carbides from KE3 SN graphites, a reduction commensurate with that seen in the overall graphite size. This may indicate that the

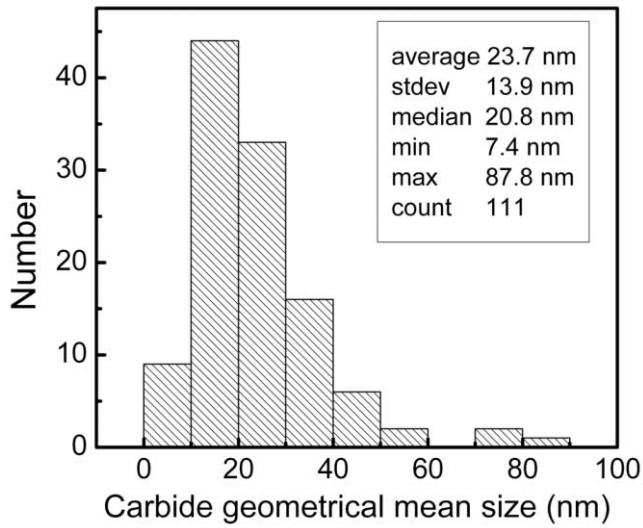

FIG. 5.—Geometrical mean size distribution of internal carbides within onion graphites. [*See the electronic edition of the Journal for a color version of this figure.*]

metal-to-carbon ratios in the gas are not radically different on average. However, there is a large variation in the relative abundance of carbides (up to 47,000 ppm), so in certain cases the transition metal–to–carbon ratio of the gas is higher. As shown in Paper II, realistic modeling of condensation in outflows from AGB stars places constraints on the allowable growth times for grains forming in circumstellar gas outflows. The gas number densities are too low to account for carbides of this size in spherically symmetric outflows, especially in cases where carbides are contained within graphites. Thus, the relatively large size of measured carbides suggests that grains condense in clumps with considerably higher density. Clumpy structures of this type have been observed in late-stage AGB stars and protoplanetary nebulae (Balick & Frank 2002).

3.4.1. *Chemical Composition of Refractory Carbides*

The mutual solid solubility of elements in the FCC carbide phase permit (Ti, Zr, Mo, Ru)C grains to form over a wide compositional range, with 1–95 at.% (atomic percent) Ti, 0–80 at.% Zr, 0–38 at.% Mo, and 0–30 at.% Ru (using a metals basis excluding carbon). The Zr, Mo, and Ru concentrations relative to Ti from EDXS measurements far exceed the solar ratios and indicate high degrees of *s*-process enrichment. Only ~12% of KFC1 carbides in onion-type graphites (13 out of 111) did not show significant *s*-process enrichment above solar values. For reference, the chemical composition of a solar composition carbide and those with 10 and 100 times solar *s*-process enrichments would be $(Ti_{99.4}Zr_{0.5}Mo_{0.1}Ru_{0.1})C$, $(Ti_{93.9}Zr_{4.4}Mo_{1.0}Ru_{0.7})C$, and $(Ti_{60.5}Zr_{28.3}Mo_{6.5}Ru_{4.7})C$, respectively. Mo and Ru are typically below the detection limit (typically 0.2–0.3 at.%) for solar composition carbides, but rise above that limit with mild *s*-process enrichments. In cases where an *s*-process element was not detected, upper limits were placed on its concentration (as described in § 2).

Unlike the *s*-process elements Zr, Mo, and Ru, other trace elements commonly seen within carbides (e.g., V, Cr, Fe, and Ni) are primarily produced via explosive Si and O burning in Type Ia and II SNe, and not in AGB stars that inherited these elements at birth. Low concentrations of V (2.8 average at.%; metals basis for this and the following concentrations) were found in many carbides, well within the allowable solid solution range for V in TiC

TABLE 2
PREDICTED CONDENSATION TEMPERATURES OF CARBIDES

log P (bars)	TiC, SOLAR	MoC, Times Solar 1	MoC, Times Solar 10	MoC, Times Solar 100	ZrC, Times Solar 1	ZrC, Times Solar 10	ZrC, Times Solar 100
−3	1862	1728 (93)	1802 (97)	1882 (101)	2026 (109)	2114 (114)	2210 (119)
−5	1702	1592 (94)	1656 (97)	1725 (101)	1867 (110)	1938 (114)	2014 (118)
−7	1564	1462 (93)	1516 (97)	1573 (101)	1725 (110)	1785 (114)	1849 (118)
−10	1370	1301 (95)	1343 (98)	1389 (101)	1547 (113)	1595 (116)	1646 (120)

NOTES.—Compilation of the predicted condensation temperatures of TiC, MoC, and ZrC at a range of pressures and *s*-process enrichments (excerpted from Lodders & Fegley 1995). The condensation temperatures of MoC and ZrC are also expressed (in parentheses) as a percentage of the TiC temperature at the same pressure.

(up to ∼34 at.% maximum). However, VC is a lower temperature condensate and thus may be strongly affected by chemical fractionation. Fe is also commonly measured within the carbides (6.5 average at.%). Iron carbide (orthorhombic) is not isostructural with the FCC carbides, but relatively large amounts (up to ∼20 at.%) can exist in solid solution within carbides. Cr was found more sporadically but sometimes in significant amounts (1.2 at.% on average; maximum of 38 at.%). Although incomplete, phase identification on the most Cr-rich grain was still consistent with a 4.4 Å unit cell FCC TiC. Ni was more rarely seen in significant amounts (maximum 9 at.%), and always along with Fe. Other elements (C, O, Si, and Ca) were present in spectra of carbides, but were also commonly measured in the graphite background, complicating accurate quantization. Grains at the most anomalous elemental compositions were confirmed as FCC carbides with microdiffraction patterns. The amounts of V and Cr within carbides were both positively correlated with Ti, likely an indication that these elements were present in the gas with uniform relative abundances.

The degree of *s*-process element enrichment (Zr, Mo, and Ru relative to Ti) within carbides is one key to revealing the stellar source of the graphites. However, chemical fractionation can alter these relative elemental abundances, depending on the condensation temperatures of the various stable phases, and such effects must first be considered. High-temperature condensates may be deficient in less refractory elements (e.g., V) if they do not equilibrate with the gas at lower temperatures. Lower temperature condensates may be deficient in more refractory elements (e.g., Zr) if these elements become depleted in the gas due to prior condensation (e.g., of ZrC). To assess the possible chemical fractionation of the major elements (Zr, Mo, and Ti), the typical condensation temperatures of these refractory carbide phases around carbon stars are needed. These have been computed for a range of reasonable pressures and C/O ratios (Lodders & Fegley 1995). ZrC has a higher condensation temperature than MoC or TiC over a wide range of C/O ratios and pressures. The predicted TiC condensation temperature is 86%–93% of that of ZrC over the ranges $1.05 < \mathrm{C/O} < 4$ and $-2 < \log P < -15$ (in bars). Over a similar range ($1.05 < \mathrm{C/O} < 2$ and $-2 < \log P < -15$), the predicted MoC condensation temperature is 80%–85% of ZrC with solar abundance ratios. With solar abundance of the metallic elements, the MoC condensation temperature is 91%–97% of that of TiC over the same range. However, *s*-process enrichments (higher than solar Mo/Ti and Zr/Ti) are clearly present in these grains, as expected for AGB environments (see § 4), and these raise the condensation temperatures of MoC and ZrC. Table 2 lists the condensation temperatures of TiC, MoC, and ZrC as a function of *s*-process enrichment above solar and pressure, all at $\mathrm{C/O} = 1.05$ (Lodders & Fegley 1995). Again, ZrC will condense first at the highest temperature at all compositions. However, with increasing degrees of *s*-process enrichment, the MoC condensation temperature rises, eventually exceeding that for TiC. Given that the average *s*-process enrichment seen in carbon stars is ∼30 times solar, the MoC and TiC condensation temperatures are rather close. Thus, the Zr/Mo and Zr/Ti ratios would be expected in some cases to show chemical fractionation, whereas this is less likely for Mo/Ti ratios. Only with the most extreme *s*-process enrichments in the gas (Mo/Ti ≫ 100 times solar) would fractionation be likely, as the predicted MoC condensation temperature rises above TiC (Lodders & Fegley 1995).

Analysis of the measured Zr/Mo ratios should give a rough indication of the degree to which chemical fractionation has occurred. Since the elemental abundance of both species will likely be equally increased by *s*-process enrichments, large deviations of the Zr/Mo ratios from the solar values are indicative of chemical fractionation. We first address whether the solar Zr/Mo number ratio of 4.6 is typical of all AGB stars. The Zr/Mo ratios vary from solar (in normal M/K giants), but decrease by roughly a factor of 2 toward S and SC giants (Abia & Wallerstein 1998). Thus if the Zr/Mo ratio is less than 50% of the solar value, this is a likely indication of chemical fractionation, with the carbide Zr/Mo ratio no longer reflecting the initial composition of the gas. Roughly half of the carbides ($N = 54$) have Zr/Mo significantly lower than this value ($\mathrm{Zr/Mo} < 2.3$), suggesting that chemical fractionation of Zr has occurred, whereas a third ($N = 36$) show Zr/Mo ratios that are roughly solar or in some cases slightly less than solar but still consistent with an AGB composition. The rest ($N = 18$) do not have sufficient Zr and/or Mo counts to make a determination. There are also six carbides (such as the larger grain in Fig. 4*b*) with slightly Zr-rich compositions ($6 < \mathrm{Zr/Mo} < 10$), again an indication of chemical fractionation. In this case, the ZrCs likely condensed at high temperature but fell out of equilibrium with the gas as the temperature decreased.

Were it not for fractionation, measurement of the Zr/Ti ratio would yield the most accurate estimate of *s*-process enrichment, due to the higher abundance of Zr. However the Mo/Ti ratios more accurately reflect the ratios in the gas and thus are used below to estimate the *s*-process enrichment. Experimental errors in the Mo/Ti EDXS ratios from counting statistics and the *k*-factor determination are relatively small (15%–45%) given the large magnitude of the enrichments. Figure 6 shows the *s*-process enrichment calculated for 80 carbides on the basis of Mo/Ti ratios that are presumed to reflect the gas composition (excluding six Zr-rich high temperature condensates and 15 carbides without measurable Mo discussed below). The *s*-process enrichments are uniformly high: the median enrichment is ∼215 times solar with

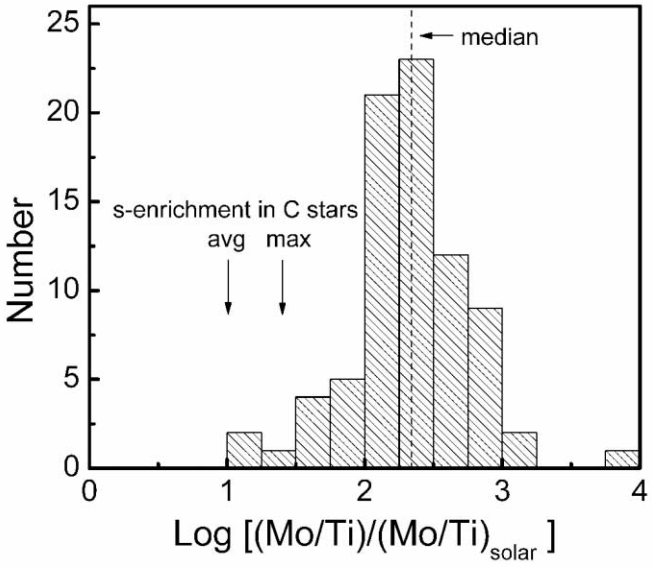

FIG. 6.—Log plot of the inferred *s*-process enrichment (derived from Mo/Ti ratios relative to solar) in carbides within onion-type graphites. The average and maximum *s*-process enrichments in AGB carbon stars are also indicated (as derived from Y and Zr in photospheric abundance spectra; Abia et al. 2002). [*See the electronic edition of the Journal for a color version of this figure.*]

a mean value of ~390 times solar (inflated by a single high measurement) and a range from ~20 to ~7950 times solar. Similarly high Mo/Ti ratios are seen in both Mo-rich carbides (relative to Zr) and in carbides with solar Zr/Mo, an indication that chemical fractionation did not strongly affect the Mo/Ti ratio. Three carbides with *s*-process enrichments above 1000 times solar were seen, but low Ti abundance gives these data large uncertainties. Roughly 85% of these carbides have *s*-process enrichments that clearly exceed the maximum enrichment (~25 times solar) observed in a large sample of AGB stars (Abia et al. 2002). The group of carbides without measurable Mo ($N = 15$) must also be considered as they represent a population of grains with lower *s*-process enrichment. Although most of these carbides could be *s*-process enriched by up to ~20 times solar, to avoid underestimating their possible effect on the overall population we can assume that all 15 carbides have solar Mo/Ti ratios. Including these 15 "solar" carbides along with the others in Figure 6, the average *s*-process enrichment is decreased by about 20% (median Mo/Ti ratio of ~174 times solar and mean value of ~330 times solar). Even with this artificially low Mo/Ti estimate for carbides without measurable Mo, the average *s*-process enrichment is not greatly reduced and still exceeds the enrichments observed in carbon stars (Abia et al. 2002).

It is useful to compare the chemical composition of these grains with other refractory carbides found within previously reported KE3 graphites of known SN origin (Croat et al. 2003). The SN graphites were identified as such based on large ^{18}O excesses, large silicon isotopic anomalies, and in some cases inferred ^{44}Ti excesses. EDXS spectra were taken from over 600 internal carbides within a dozen graphites. In all 600+ carbides, no *s*-process elements (Zr, Mo, or Ru) were ever seen above the detection limit, in sharp contrast to the ~90% of KFC1 carbides that show *s*-process enrichments. Moreover, the KE3 SN carbides were also larger on average, which would have improved the ability to measure trace concentrations. The average upper limits for *s*-process enrichment relative to solar ratios in larger KE3 carbides ($N = 214$) were 0.5, 2.7, and 3.5 times solar for Zr, Mo, and Ru, respectively. Two SN graphites (KE3e3 and KE3e11) had many smaller internal carbides ($N = 411$) with an average diameter (~30 nm) similar to that of the KFC1 carbides. Again no *s*-process elements were measured, with average upper limits of 2, 9, and 12 times solar for Zr, Mo, and Ru, respectively. These observations give us confidence that the *s*-process enrichments in KFC1 carbides reflect the composition of the gas rather than the degree of elemental fractionation during condensation. If chemical fractionation alone were capable of producing enrichments in more refractory *s*-process elements, one would expect to observe those elements (which are not seen) in at least *some* of the hundreds of SN carbides that were analyzed.

3.4.2. *NanoSIMS Analyses of Carbide-containing Graphites*

NanoSIMS isotopic measurements have been made on several of the carbide-containing graphites. Such combined isotopic and TEM microstructural studies can extract the maximum amount of information from single grains, revealing both their stellar source and formation conditions. These measurements were not optimized for maximum spatial resolution, so the internal carbides themselves were not visible in the isotopic image maps. Figure 7 shows the carbon and oxygen isotopic ratios for some of the onion-type graphites that contained carbides. These are grouped according to the degree of *s*-process enrichment as inferred from the chemical composition of the internal carbides. The isotopic ratios of the carbide-containing graphites fall within the normal range for KFC1 graphites (see Fig. 1), with most in the $100 < {}^{12}C/{}^{13}C < 400$ range. Only one of the carbide-containing graphites is in the ^{12}C-poor group ($^{12}C/^{13}C = 11 \pm 4$). Its internal carbide is a pure TiC: no *s*-process elements were measured, and upper limits on *s*-process enrichment are 3 and 14 times solar for Zr and Mo, respectively. Another pure TiC was found in a graphite with a higher than solar $^{12}C/^{13}C$ ratio (of 340 ± 8) and a possible oxygen isotope anomaly. However, there are insufficient counts to clearly show an anomaly (1 σ errors for $^{16}O/^{18}O$ are plotted). The graphites containing carbides with moderate and high *s*-process enrichments (*circles and squares, respectively*) are all ^{12}C rich relative to the solar composition and lack large oxygen anomalies. Two graphites from the moderate *s*-process enriched group may have mild ^{18}O excesses (greater than 2 σ deviation below solar ratio). The degree of *s*-process enrichment does not correlate with isotopic anomalies in carbon or oxygen,

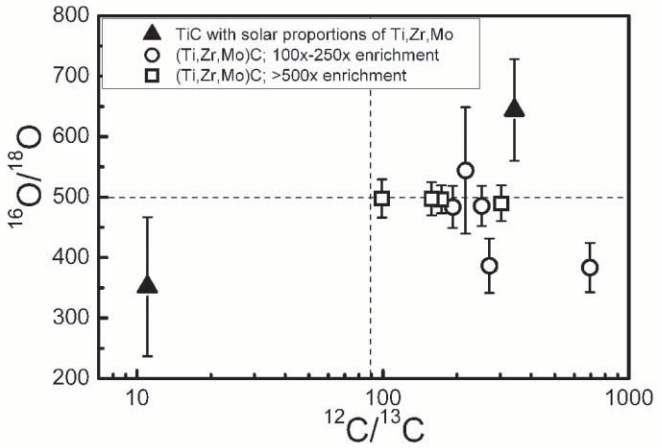

FIG. 7.—Carbon and oxygen isotopic measurements of KFC1 carbide-containing onion graphites with the NanoSIMS, with 1 σ error bars for oxygen (carbon error bars are smaller than the plotted symbol). Graphites are grouped according to degree of *s*-process enrichment as inferred from the chemical composition of their internal carbides. [*See the electronic edition of the Journal for a color version of this figure.*]

and graphites with the largest *s*-process enhancements appear to have $^{16}O/^{18}O$ ratios that are clearly solar and lack extreme carbon anomalies. The KFC1 graphites appear to lack the large ^{18}O excesses seen in the KE3 SN graphites, although the counting statistics do not rule out mild oxygen anomalies. Considerable oxygen was present within the graphites, with an average $^{12}C/^{16}O$ count ratio of ~10. However, the limited amount of material available in a single TEM slice complicates isotopic measurements of minor elements such as oxygen.

3.5. *Other Phases within Onion Graphites*

Other mineral phases besides carbides were also occasionally found within graphites, including metallic iron, iron carbide, and even a metallic osmium-rich phase. As described below, models of the thermodynamics of grain condensation suggest that it is unlikely that these phases would form before graphite around carbon stars with solar proportions of these elements. In this small number of cases, a SN origin is more likely. Thus, a diversity of stellar sources is required to explain the observed mineralogy of all of the KFC1 presolar graphites.

Four iron-rich grains were found within individual onion-type graphites. Two of these were confirmed as kamacite (2.9 Å bcc phase) using microdiffraction patterns. The kamacites have low Ni content (3–4 at.%), and traces of Cr and S were seen in one spectrum. The spectra from the remaining two are strongly suggestive of kamacite, again with low Ni content (3 and <1 at.% Ni) and no other elements not attributable to the graphite background. An iron carbide [hexagonal $(Fe, Cr)_7C_3$ phase] was also identified within one onion graphite. Electron microdiffraction is required to distinguish between Fe-metal and Fe-carbide phases, since the EDXS measurements are made in a sea of carbon. Four microdiffraction patterns were taken that are consistent with a hexagonal phase with lattice parameters of $a = 7.1$ Å and $c = 4.8$ Å (using graphite ring spacings for calibration). It is clearly not any of the metallic Fe phases, which all have <3.7 Å lattice parameters. Fortuitously, two low-index hexagonal zones ([0 0 0 1] and [2 −1 1 0]) were identified at 90° angular separation from each other, an unambiguous indication of a hexagonal structure. The (0 0 0 1) diffraction spots were also visible, indicating that the phase was not close-packed hexagonal, although the exact space group has not been determined. The crystal structure and composition of this grain are a good match to a known hexagonal $(Fe, Cr)_7C_3$ phase, with $a = 6.95$ Å, $c = 4.5$ Å. The lattice parameters of the iron-chromium carbide are 2% and 6% larger than the known phase for *a* and *c*, respectively. The bulk metal composition of the grain is $Fe_{73}Cr_{21}Ti_6$, although there are indications of a smaller region in the center with lower Cr and Fe more similar in composition to refractory carbides (Bernatowicz et al. 1996). No evidence was seen during tilting experiments for a separate carbide subgrain, although surface contaminations from previous TEM examinations may have obscured any observations of substructure. If the grain did consist of a smaller central carbide overgrown with iron-chromium carbide, the inferred condensation sequence (TiC → iron-rich phase → graphite) would be similar to the TiCs with iron subgrains found within SN graphites (Croat et al. 2003). The Cr/Fe ratio of the grain (~0.29) is lower than the reported range of the $(Fe, Cr)_7C_3$ phase ($0.5 < Cr/Fe < 3$). However, the $(Fe, Cr)_7C_3$ phase is virtually isostructural with Fe_7C_3 (hexagonal; $a = 6.68$ Å, $c = 4.54$ Å; $P6_3/mc$), so the solubility range may be wider than reported, enough to encompass the observed grain composition.

Despite the low cosmic abundance of osmium ([Os/H] = 1.4), a metallic osmium-rich grain was found within an onion graphite (Fig. 4*c*). This grain was relatively large (~50 nm) and had an approximate chemical composition of $Os_{79}Mo_{10}Ru_9Fe_2$. Five microdiffraction patterns from this grain (including the low-index [0 1 −1 0] and [−1 2 −1 0] zones separated by 30°) were indexed to a hexagonal close-packed crystal structure with $a = 2.77 \pm 0.05$ Å and $c = 4.45 \pm 0.09$ Å. This is a good match for a known metallic osmium-ruthenium phase ($a = 2.73$ Å, $c = 4.31$ Å), with a larger *c*-axis lattice parameter by ~3%. The only reported osmium carbide is also hexagonal, but is a tungsten-carbide type phase with $a = 2.91$ Å and $c = 2.82$ Å.

Unlike the early transition metals (e.g., Ti, V, Zr), which are only found within carbides, the group VIII transition metals (Fe, Ru, Os) commonly form metallic phases within graphites (the one exception being the iron carbide mentioned above). Metallic ruthenium-iron phases (Ru_xFe_{1-x} with $0.66 < x < 0.77$) have been found previously in several cauliflower graphites (Croat et al. 2004). Iron-rich phases (both kamacite and taenite) were found within SN graphites, normally as subgrains attached to TiCs but also occasionally as independent grains (Croat et al. 2003). To our knowledge, this is the first report of both iron-rich carbides and metallic osmium grains within presolar grains. NanoSIMS isotopic measurements on the graphites containing these new presolar phases have not yet been made.

Notable mostly by their absence, SiC grains were not found within hundreds of KFC1 graphites. Due to their nearly identical structures (4.35 Å FCC vs. 4.39 Å FCC), SiC and TiC are difficult to distinguish from crystal structures alone. A few SiC candidates were found within the population of very small internal grains without measurable Ti in weak EDX spectra. However, on further investigation small amounts of Zr were always found, suggesting these may be *s*-process enriched carbides rather than SiC. As mentioned previously, Si is difficult to quantify due to its presence in the graphite background, so distinguishing between small ZrC and SiC grains is difficult. Only one internal SiC grain within graphite has been reported previously (Bernatowicz et al. 1996), and as discussed by those authors, this virtual absence of SiC within graphite is consistent with the condensation sequence predicted by equilibrium thermodynamics (also Paper II).

4. DISCUSSION

Since AGB stars are known as the primary sites for *s*-process nucleosynthesis (Busso et al. 1999), the large enrichment in *s*-process elements as well as several lines of isotopic evidence (see Paper II) conclusively establish that most (~90%) carbide-containing graphites clearly form in the circumstellar environment of AGB stars with C > O (carbon stars). Resonant ionization mass spectrometry (RIMS) of Zr and Mo isotopes support an AGB origin for some KFC1 graphites, with *s*-process isotopic signatures found within eight graphites, presumably with the signal coming from internal carbides (Nicolussi et al. 1998c). Zr isotopic patterns were typically more anomalous than Mo, with deviations of up to an order of magnitude in the $^{96}Zr/^{94}Zr$ ratio. Most of the rest did not show anomalies, possibly due to lower carbide abundance in these graphites. There were also two graphites showing ^{96}Zr excesses, suggesting either an *r*-process origin or an *s*-process origin with unusually high neutron exposure. However, neither the chemical compositions of the internal carbides nor their abundance within each graphite were known.

Even given an AGB stellar source, the *s*-process enrichments astronomically observed in carbon stars in general do not appear to be sufficiently large to produce the *s*-enriched carbides studied here. Numerous *s*-process elements (including Y, Zr, La, and Ba) have been observed in carbon star photospheric spectra, and their enrichment is inferred based on the strength of these lines relative to Ti or Fe. Zr/Ti ratios of up to ~158 times solar (with a

mean enrichment of ~29 times solar) were measured in the photospheric spectra of 36 carbon stars (Utsumi 1970, 1985). Even higher enrichments were also found in heavier *s*-process elements (e.g., Ba, La, Nd, and Sm, and denoted as "hs") as opposed to the lighter ones (e.g., Y, Zr, and Mo, and denoted as "ls"). One C star (Y CVn) was reported to have more extreme *s*-process enrichment (~200 times solar Zr and ~4000 times solar La enrichments with respect to iron; Fujita & Tsuji 1965), although this was later disputed by Kilston (1975), who found much smaller *s*-process enrichment in the same star (~6 times solar Zr enrichment relative to Fe). Such large discrepancies raise questions about the model dependence of the results and suggest that such determinations from photospheric spectra should be used as relative measures of elemental abundance among carbon stars rather than giving precise values (Gustafsson 1989). More recent studies (Abia et al. 2002), with higher resolution photospheric spectra on numerous N-type carbon stars, yield lower *s*-process enrichments (maximum ~16 times solar enrichment in light *s*-elements and mean value of ~5 times solar, which roughly correspond with Zr/Ti ratios of ~25 times solar for the maximum and ~10 times for the mean). These recent measurements of the same carbon stars from the Utsumi study yield lower *s*-process enrichments, up to an order of magnitude lower in one case. Higher *s*-process enrichments are seen in post-AGB stars, with up to ~100 times solar enrichments in light *s*-elements (Reyniers et al. 2004), an indication that *s*-process elements can become progressively more enriched over the course of C-star evolution. Although such photospheric abundance studies are scarce, no unambiguous enrichments in light *s*-process elements (e.g., Zr, Mo, Ru) of sufficient magnitude to match those seen in presolar carbides have been astronomically observed.

Much effort has gone into the development of realistic models capable of reproducing the observed abundances of the full spectrum of *s*-process elements. The slow, sustained neutron source required to drive the *s*-process is present in helium intershell region of thermally pulsing AGB stars. The $^{13}C(\alpha, n)^{16}O$ reaction (within ^{13}C pockets) provides the primary neutron source necessary to convert Fe seeds to the *s*-process elements in lower mass AGB stars (~1–3 $M_{\odot}$). It is believed that within these ^{13}C pockets, after the depletion of the ^{13}C neutron source, local *s*-process enrichments of up to 1000–50,000 times solar will exist (Gallino et al. 1997). These *s*-process elements (along with large amounts of ^{4}He and ^{12}C from 3α He burning) are then transported to the surface by third dredge-up events, as was made clear by the observation of short-lived Tc on the stellar surface (Merrill 1952). After repeated thermal pulses and the accompanying dredge-up events, ^{12}C from the He burning shell continually enriches the outer envelope in C, creating a carbon star (C > O). That ^{12}C (and not ^{13}C) contributes most of the carbon is clear, because N and O anomalies from the CNO cycle that would accompany ^{13}C are not seen (Lambert et al. 1986). For this reason one might expect higher $^{12}C/^{13}C$ ratios in regions with highest C/O, which is also the condition under which graphite formation is most likely to occur. Since ^{12}C and *s*-process elements are dredged up together, there is a natural correlation between light carbon isotopic anomalies and *s*-process elements, especially so due to the ^{13}C destruction during the *s*-process. Although later mixing will affect these compositions, the possibility of a less completely mixed region that preserves the larger enrichments must be considered.

Recent observations and modeling have suggested that *s*-process overabundances could be even greater in low-metallicity AGB stars (Busso et al. 2001). The size of the neutron-producing pocket [and thus the overall neutron flux from $^{13}C(\alpha, n)^{16}O$] is not greatly affected by a star's metallicity. The number of Fe seed nuclei, though, obviously decreases with metallicity, raising the neutron flux per iron seed and leading to higher *s*-process elemental abundance relative to lighter non–*s*-process metals (e.g., Ti). Such a metallicity difference may begin to explain the carbides with large *s*-enrichment. However, there are difficulties with postulating a lower metallicity origin. Lower metallicity would necessarily lead to lower number densities of metals in the outflowing gas, which already appear to be too low to form large carbides in spherically symmetric AGB outflows (as described in Paper II). Also, the high neutron flux per seed nucleus is predicted to lead to greater abundances for heavy *s*-elements (Pb at lowest metallicity and Ba at intermediate metallicity) partially at the expense of the light *s*-elements (Y, Zr, Mo, etc.). The Zr peak elements become more important at metallicities above $[Fe/H] \sim -0.8$ (Busso et al. 1999). There is also considerable diversity in the observed *s*-process abundance in the photosphere as a function of metallicity, suggesting that other variables (such as the severity of the dredge-up) affect the amount that escapes to larger radii where grain condensation occurs.

Along with the *s*-process enrichments, the carbon isotopic ratios are also important to understanding the origin of these graphites. The isotopic composition of the photospheres of most carbon stars is subsolar, peaking in the $30 < {}^{12}C/{}^{13}C < 70$ range (Lambert et al. 1986). There is also a considerably smaller population of ^{13}C-rich stars ($^{12}C/^{13}C \sim 4$). This distribution matches well with mainstream presolar SiCs, but not with the isotopically light graphites observed in this study. The C isotopic ratio is determined by the relative contributions of the 3α process (^{12}C production) and the CNO cycle (^{13}C production) in thermally pulsing AGB stars. As mentioned above, there is a natural correlation between ^{12}C and the *s*-process elements as both are produced near the thin He burning shell of AGB stars (with the ^{13}C *s*-producing pocket being just above this layer) and both are dredged up together. Although dredged-up ^{12}C raises the photospheric $^{12}C/^{13}C$ ratio, it remains below the solar ratio due to the large amounts of ^{13}C in the envelope from the first dredge-up. Observational evidence confirms the ^{12}C enrichment, because on average higher $^{12}C/^{13}C$ ratios are found in later stage carbon stars, compared with M and S stars (Smith & Lambert 1990). In larger AGB stars, the C isotopic ratio can be lowered after the dredge-up events due to the CNO cycle at the base of the envelope (similar to the cool bottom processing seen in red giant stars and inferred from oxygen isotope composition in some presolar oxides; Wasserburg et al. 1995).

Assuming a limited role for fractionation (as argued in § 3.4), the high *s*-process enrichments and the light carbon isotopes in carbide-containing graphites suggest that some of the dredged-up material may escape from the stellar envelope before being completely mixed within the outer envelope. Paper II concludes that carbide and graphite formation in AGB outflows requires higher than average density, such as would be found in clumps or jets of small solid angle. With such spatially inhomogeneous outflows, it is also possible that these regions are also chemically and isotopically inhomogeneous. Any such inhomogeneous regions with light carbon and high *s*-process enrichment may not be readily detectable by astronomical observations. Photospheric observations of carbon stars (especially in their later stages) are not only rare, but also cannot spatially resolve any inhomogeneities in chemical or isotopic composition. Spatially averaged and time-averaged C isotopic ratios and *s*-process abundances may thus not reflect the conditions at the time and place of graphite formation. On the basis of AGB models that consider both the mixing and mass loss processes, it is unclear whether a relatively unmixed region of gas could reasonably escape from the envelope,

but this may be possible at the higher mass-loss rates obtained in late-stage AGB stars. Observations of carbon stars with discrete periods of considerably higher mass loss, presumably caused by thermal pulses, offer a possible scenario in which this could occur (Olofsson et al. 1996).

Silicon carbide is another common presolar phase believed to form primarily in carbon stars, because mainstream SiC grains match the carbon isotopic ratios seen in carbon stars, show evidence of *s*-process nucleosynthesis, and require carbon-rich environments (C > O) to form. Trace element abundance patterns in mainstream SiCs have shown slight *s*-process enrichments, up to 14 times solar with respect to Ti (Amari et al. 1995). However, slight chemical enrichments are more difficult to measure accurately than in titanium carbides, since the *s*-process elements predominantly condense into refractory phases with little remaining to be incorporated at lower temperatures in SiCs. More recently, RIMS isotopic measurements have shown large and variable *s*-process signatures in Zr, Mo, Sr, and Ba in presolar SiC (Nicolussi et al. 1997, 1998a, 1998b; Savina et al. 2003). In some cases, nearly pure *s*-process isotopic signatures are seen, whereas others have an *s*-process component mixed with a solar-like component. Despite some similarities with KFC1 graphites, the substantially different carbon isotopic ratios show that SiC grains do not simply form at a slightly lower temperature from the same type of outflows that form graphite. SiC appears to form from carbon star outflows that are more chemically and isotopically homogenous, whereas graphite appears closer in chemical and isotopic composition to the products of the thermally pulsing regions. Also, due to their higher *s*-process enrichment and lighter carbon isotopes, graphites may form later in the course of carbon star evolution.

Despite the origin of most KFC1 graphites in AGB stars, there is a subset of graphites with more rare internal phases that are suggestive of a SN origin. The graphite containing metallic osmium is unlikely to form in AGB outflows due to kinetic limitations on Os grain growth. Using the methods of Paper II, the maximum size to which an osmium grain could grow in AGB outflows can be estimated, and the resulting size is over 4 orders of magnitude too low (assuming solar abundances). Slightly higher Os abundances ($\sim$20 times solar) have been observed around chemically peculiar stars (Ivarsson et al. 2004), but this still leaves a considerable discrepancy. Os is known as a predominantly *r*-process element (Cowan et al. 1996), and for this reason the osmium-containing graphite more likely originates in a stellar source that is very active in the *r*-process, such as a SN.

Unlike TiC or metallic osmium, grains of iron-rich phases (kamacite or iron carbide) do not face the same kinetic limitations on their ultimate size, due to the higher gas number density of iron. However, according to thermochemical models, condensation of iron-rich phases before graphite will not occur at reasonable pressures and C/O ratios with a solar Fe/C ratio. Thus, the observation of these iron phases within graphites implies a significant overabundance of iron relative to carbon. This required iron overabundance can be roughly estimated, based on the predicted condensation temperatures from Lodders & Fegley (1995). If the iron-containing graphites form at the upper end of the range of reasonable pressures ($\sim 10^{-4}$ bars) and with lower C/O ratios (C/O = 1.05), they would require $\sim$100 times solar enrichment in Fe relative to C for iron phases to form before graphite. The iron overabundance would have to be higher still in gases with higher C/O ratios or lower total pressures. Given the difficulty in reaching such enrichments in AGB circumstellar environments, and the presence of iron phases within graphites of SN origin (Croat et al. 2003), a SN origin is possible for KFC1 graphites with internal iron grains. However, NanoSIMS isotopic data are not yet available for iron-containing graphites.

No conclusions are made at this time regarding the stellar source of graphite slices without internal grains or graphites containing pure TiCs (no *s*-process elements). The pure TiCs are consistent in chemical composition with those found within SN graphites. However, these graphites appear to lack the oxygen isotopic anomalies seen in SN graphites, although uncertainties from poor counting statistics are still considerable.

5. SUMMARY AND CONCLUSIONS

Correlated TEM and NanoSIMS investigations have revealed for the first time that both isotopically light carbon anomalies and high *s*-process enrichments are present in the same graphites. The *s*-process enrichments (as inferred from the Mo/Ti ratio in internal carbides) suggest an AGB origin for most KFC1 graphites, and these enrichments are likely not greatly altered by chemical fractionation. Despite the AGB origin, the light carbon anomalies and the *s*-process enrichments both exceed the values astronomically observed in AGB photospheres. There is a natural correlation between ^{12}C and *s*-process elements due to their formation in and dredge-up from the He intershell region of AGB stars. The confluence of isotopically light carbon, high *s*-process enrichments, and the required high-density knots or jets in the circumstellar outflows (addressed in Paper II) raises the possibility that these graphites condense in both chemically and isotopically inhomogeneous regions around AGB stars.

Despite the predominant AGB carbon star origin of most KFC1 graphites, a subset containing rare internal phases (e.g., iron carbide, metallic osmium) is more consistent with a supernova origin. Kinetic or thermochemical limitations on the formation of such grains within graphites suggest that they are unlikely to occur in AGB circumstellar outflows with solar-like composition. The required elemental overabundances (e.g., of Fe or Os) are more likely to occur in the outflows from supernovae.

This material is based on work supported by NASA under grant NNG04GG13G issued through the Office of Space Science.

REFERENCES

Abia, C., & Wallerstein, G. 1998, MNRAS, 293, 89
Abia, C., et al. 2002, ApJ, 579, 817
Amari, S., Hoppe, P., Zinner, E., & Lewis, R. S. 1993, Nature, 365, 806
———. 1995, Meteoritics, 30, 679
Amari, S., Lewis, R. S., & Anders, E. 1994, Geochim. Cosmochim. Acta, 58, 459
Balick, B., & Frank, A. 2002, ARA&A, 40, 439
Bernatowicz, T. J., Akande, O. W., Croat, T. K., & Cowsik, R. 2005, ApJ, 631, 988 (Paper II)
Bernatowicz, T. J., Cowsik, R., Gibbons, P. C., Lodders, K., Fegley, B., Jr., Amari, S., & Lewis, R. S. 1996, ApJ, 472, 760
Busso, M., Gallino, R., Lambert, D. L., Travaglio, C., & Smith, V. V. 2001, ApJ, 557, 802
Busso, M., Gallino, R., & Wasserburg, G. J. 1999, ARA&A, 37, 239
Clayton, R. N., & Nittler, L. 2004, ARA&A, 42, 39
Cowan, J., Sneden, C., Truran, J. W., & Burris, D. L. 1996, ApJ, 460, L115
Croat, T. K., Bernatowicz, T., Amari, S., Messenger, S., & Stadermann, F. J. 2003, Geochim. Cosmochim. Acta, 67, 4705
Croat, T. K., Stadermann, F. J., Zinner, E., & Bernatowicz, T. J. 2004, Lunar Planet. Sci., 35, 1353
Fraundorf, P., & Wackenhut, M. 2002, ApJ, 578, L153
Fujita, Y., & Tsuji, T. 1965, Publ. Dom. Astrophys. Obs., 12, 339

Gallino, R., Busso, M., & Lugaro, M. 1997, in Astrophysical Implications of the Laboratory Study of Presolar Materials, ed. T. J. Bernatowicz & E. Zinner (New York: AIP), 115
Gustafsson, B. 1989, ARA&A, 27, 701
Hoppe, P., Amari, S., Zinner, E., & Lewis, R. S. 1995, Geochim. Cosmochim. Acta, 59, 4029
Ivarsson, S., Wahlgren, G. M., Dai, Z., Lundberg, H., & Leckrone, D. S. 2004, A&A, 425, 353
Jaszczak, J. A. 1995, in Mesomolecules: From Molecules to Materials, ed. G. D. Mendenhall, A. Greenberg, & J. F. Liebman (New York: Chapman & Hall), 161
Kilston, S. 1975, PASP, 87, 189
Lambert, D. L., Gustafsson, B., Eriksson, K., & Hinkle, K. H. 1986, ApJS, 62, 373
Lodders, K., & Fegley, B., Jr. 1995, Meteoritics, 30, 661
Merrill, P. W. 1952, ApJ, 116, 21
Nicolussi, G. K., Davis, A. M., Pellin, M. J., Lewis, R. S., Clayton, R. N., & Amari, S. 1997, Science, 277, 1281
Nicolussi, G. K., Pellin, M. J., Lewis, R. S., Davis, A. M., Amari, S., & Clayton, R. N. 1998a, Geochim. Cosmochim. Acta, 62, 1093
Nicolussi, G. K., Pellin, M. J., Lewis, R. S., Davis, A. M., Clayton, R. N., & Amari, S. 1998b, Phys. Rev. Lett., 81, 3583
———. 1998c, ApJ, 504, 492
Olofsson, H., Bergman, P., Eriksson, K., & Gustafsson, B. 1996, A&A, 311, 587
Reyniers, M., Van Winckel, H., Gallino, R., & Straniero, O. 2004, A&A, 417, 269
Savina, M. R., et al. 2003, Geochim. Cosmochim. Acta, 67, 3201
Smith, V. V., & Lambert, D. L. 1990, ApJS, 72, 387
Stadermann, F. J., Croat, T. K., Bernatowicz, T. J., Amari, S., Messenger, S., Walker, R. M., & Zinner, E. 2005, Geochim. Cosmochim. Acta, 69, 177
Utsumi, K. 1970, PASJ, 22, 93
———. 1985, Proc. Japan Acad., 61B, 193
Wasserburg, G. J., Boothroyd, A. I., & Sackmann, I.-J. 1995, ApJ, 447, L37
Zinner, E. 1998, Annu. Rev. Earth Planet. Sci., 26, 147